

New methods to assess and improve LIGO detector duty cycle

A Biswas^{1,2,6}, J McIver^{2,3}, and A Mahabal^{2,4,5}

¹IIT Gandhinagar, Gandhinagar, Gujrat 382355, India

²LIGO Laboratory, California Institute of Technology, Pasadena, CA 91125, USA

³University of British Columbia, Vancouver, Canada

⁴Division of Physics, Mathematics, and Astronomy, California Institute of Technology, Pasadena, CA 91125, USA

⁵Center for Data Driven Discovery, California Institute of Technology, Pasadena, CA 91125, USA

⁶University of California San Diego, 9500 Gilman Dr, La Jolla, CA 92093, USA

Abstract. A network of three or more gravitational wave detectors simultaneously taking data is required to generate a well-localized sky map for gravitational wave sources, such as GW170817. Local seismic disturbances often cause the LIGO and Virgo detectors to lose light resonance in one or more of their component optic cavities, and the affected detector is unable to take data until resonance is recovered. In this paper, we use machine learning techniques to gain insight into the predictive behavior of the LIGO detector optic cavities during the second LIGO-Virgo observing run. We identify a minimal set of optic cavity control signals and data features which capture interferometer behavior leading to a loss of light resonance, or *lockloss*. We use these channels to accurately distinguish between lockloss events and quiet interferometer operating times via both supervised and unsupervised machine learning methods. This analysis yields new insights into how components of the LIGO detectors contribute to lockloss events, which could inform detector commissioning efforts to mitigate the associated loss of uptime. Particularly, we find that the state of the component optical cavities is a better predictor of loss of lock than ground motion trends. We report prediction accuracies of 98% for times just prior to lock loss, and 90% for times up to 30 seconds prior to lockloss, which shows promise for this method to be applied in near-real time to trigger preventative detector state changes. This method can be extended to target other auxiliary subsystems or times of interest, such as transient noise or loss in detector sensitivity. Application of these techniques during the third LIGO-Virgo observing run and beyond would maximize the potential of the global detector network for multi-messenger astronomy with gravitational waves.

1. Introduction

Gravitational waves, small ripples in the fabric of spacetime, are able to probe the inner dynamics of highly energetic systems that are difficult to directly observe via electromagnetic radiation. The LIGO and Virgo collaborations have reported the detection of gravitational waves from the merger of ten binary black hole (BBH) systems [1], and one binary neutron star (BNS) merger [2] from their first and second observing runs. Four of these signals were identified in and analyzed across a global network of three dual-recycled Michelson gravitational wave interferometers: two LIGO detectors in the U.S. and Virgo in Italy [3, 4]. This global network enabled sky localization for three signals (GW170814, GW170817, GW170818) on the order of tens of square degrees, with

the BNS event (GW170817) localized to just 16 square degrees [1]. The skymap produced for GW170817 resulted in the identification of the host galaxy [5, 6], which was the first example of multi-messenger astronomy with gravitational waves, and resulted in a broad array of advances in astrophysics [7, 8].

Maximizing observatory uptime is critical to achieving a high rate of confident detections and producing an accurate skymap with the broadest array of detectors in the global network. The LIGO and Virgo detectors are in the midst of the third Advanced-era observing run (O3). Detector sensitivity is significantly higher than during O2; LIGO-Livingston has achieved an average sensitivity of over 130 Mpc, LIGO-Hanford of over 100 Mpc, and Virgo of just under 50 Mpc [9]. KAGRA is expected to join O3 toward the end of the observing run. The combined network was expected to detect as many as one significant GW event every week [10], and the LIGO-Virgo Collaboration has released more than one un-retracted candidate event per week via public alerts on average since the start of the run. This three detector network has reported sky localizations for candidate events as low as tens of square degrees during O3 [11]. However, ground-based gravitational wave detectors such as LIGO and Virgo are susceptible to loss in observation time, often due to elevated ground motion, including earthquakes, winds, microseism and anthropogenic activity.

Prior studies have shown a direct correlation between the ground velocity and *lockloss* events, when one or more optical cavities lose light resonance [12, 13]. For example, control of the component optic cavities within the detector becomes unstable at higher ground velocities. It can take several hours for a detector to return to its operating state after an earthquake, and high winds or high microseism may also prevent a stable detector control state. The LIGO detectors also record the time series of power circulating within optic cavities and time series used to monitor and control cavity length and the relative angle of the component optics. By using information recording in these *auxiliary channels*, we can infer which components of a detector are more susceptible to losing light resonance and causing a lockloss.

In recent years, machine learning has been employed to characterize noise in the LIGO and Virgo detectors, including the identification of glitches [14, 15, 16, 17], the correlation of glitches with auxiliary witness sensors [18, 19, 20], and a novel approach that blends citizen science with convolutional neural nets [21, 22]. Deep learning methods in particular have been instrumental in characterizing rich structure in data that has lead to new insights into instrument behavior [23]. Deep learning methods internally explore millions of features and internally downselect a subset that provide the best discrimination [24]. This is in contrast to tens to hundreds of features that humans might handpick. While these handpicked domain knowledge assisted features are often a great start, they also tend to be biased and almost always incomplete. Deep learning supplements these with complex features directly derived from the data. In this study we explore deep learning techniques to understand complex nonlinear interaction of auxiliary channels preceding lockloss events, with the goal of improving the duty cycle of the global interferometer network.

In this paper we present results using O2 data to illustrate the effectiveness of three different machine learning approaches with different strengths to improve our understanding of why the Advanced LIGO interferometers lose lock. In Section 2 we describe our approach, including the data, machine learning techniques, event selection, and feature selection used. In Section 3 we present our results. In Section 4 we discuss our results and outline future targets for this effort as the LIGO and Virgo detectors enter their third observing run.

2. Approach

2.1. Auxiliary channel data

The LIGO detectors record data from roughly 200,000 auxiliary channels that witness the behavior of the detectors’ subsystems and local environment [25, 26]. To limit the computational expense of our analysis, we downselected to 22 channels, including ground motion sensors that witness seismic events and channels used to sense and control the optics comprising the major resonant cavities in the interferometer.

For ground motion witnesses, we chose auxiliary channels that would form a minimal basis set to distinguish between different sources of seismic events. Based on the prior finding that LIGO detector lockloss mechanisms include ground motion [12], we investigated the following potential sources of seismic-related locklosses: earthquakes, high wind, high microseismic ground motion, and anthropogenic noise in the 10-30 Hz band, which captures ground motion due to nearby human activity such as snow removal at the LIGO-Hanford site. For all ground motion witness channels, we used the array of Streckeisen STS-2s sensors at both LIGO sites [27]. Since higher frequency ground motion tends to be highly localized and change rapidly, we included downsampled second-trends of channels that witnessed 10-30 Hz vertical ground motion at the two end stations which house the optics used for one end of each of the interferometer arms, and the *corner station*, which houses the input laser, beam splitter, auxiliary optics, and data readout. To distinguish between earthquake events, which manifest in vertical and horizontal ground motion at low frequencies, and wind, which manifests largely in horizontal ground motion in the same frequency band, we included a second-trend of 0.03-0.1 Hz vertical ground motion and another witnessing horizontal ground motion in the same frequency band. To capture microseismic ground motion, we also included a downsampled minute-trend of 0.1-0.3 Hz vertical ground motion [28].

For interferometer optic cavity control channels, again based on prior knowledge of potential lockloss mechanisms, we chose a channel set that spanned different degrees of freedom used to actively stabilize cavities both in length and relative angle. To target length sensing and control, we included a witness of power in the Input Mode Cleaner (IMC), power in the Power Recycling Cavity (POP), and light reflected from the Power Recycling Mirror (REFL). We also included length control signals of the inner Michelson interferometer (MICH), the Power Recycling Cavity (PRCL), and the Signal Recycling Cavity (SCRL), as shown in Figure 1. To target alignment sensing and control, we included control signals for the ‘pitch’ and ‘yaw’ degrees of freedom for the common and differential modes of the interferometer, and the ‘hard’ and ‘soft’ relative optics orientations of each (see Figure 16 of [3]).

For each of the 22 auxiliary channels we studied, we considered time-series of a fixed duration before lockloss. We then extracted several features described in the next Section (e.g. *dmdt* mappings, spectrograms and various statistical features) from the time-series data. We applied a variety of machine learning techniques on these computed features to visualize differences in behavior as clusters and classified the inputs into two classes: lockloss or quiet (non-lockloss).

2.2. Machine learning tools used

LIGO auxiliary channel data are regular and continuous timeseries data. High data sampling rates of the 22 selected channels (up to 512 Hz) motivated additional data volume reduction through systematic pre-processing before passing the data to machine learning tools. Of the many machine learning techniques available, we chose to focus on three: (a) random forests (RF; stable and fast

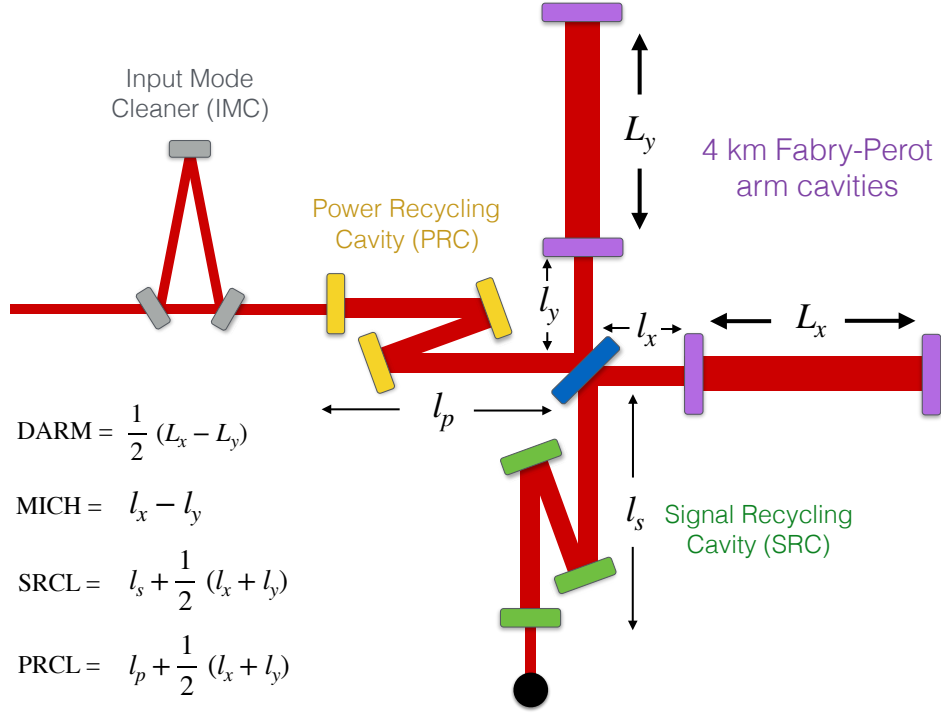


Figure 1: Simplified schematic of the basic Advanced LIGO interferometer layout, illustrating how differential arm length (DARM), the inner Michelson interferometer (MICH), the Signal Recycling Cavity Length (SRCL) and Power Recycling Cavity Length (PRCL) are calculated relative to the position of the beam splitter optic, shown in blue.

supervised learning [29]), (b) convolutional neural networks (CNNs; supervised deep learning [24]), and (c) t-distributed stochastic neighbour embedding (t-SNE; unsupervised clustering [30]). We describe below each of the tools, the data features used, and the preprocessing applied.

2.2.1. Random forest Random forest (RF; [29]) is an ensemble learning method where a large number of decision trees are constructed with various subsets of a set of features derived from the input data. The output of RF classification is the mode of the answer given by each decision tree. We used several simple statistical features which have been used for the classification of astronomical light curves [31], as detailed in Table 1. Choosing a few tens of features has the advantage that each time-series gets reduced from hundreds of thousands of points to just several summary numbers. We note that handcrafting the features is a common practice to improve classification accuracy, but this can also lead to a bias and non-generality. An alternative is to obtain hundreds to thousands of summary statistics, and then use dimensionality reduction techniques to bring the number down for a given problem. This too can introduce some subjectivity. Given that the time-series we have are non-sparse, regular, and continuous, we found using the several standard statistical features

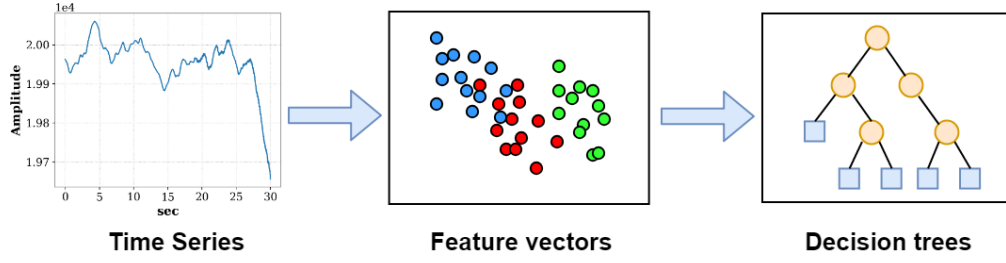


Figure 2: Work-flow for classification with random forest. The left panel shows a time-series, the middle panel depicts features derived from the time-series (such as those described in Table 1), and the right panel shows a series of possible decision trees that determine the likely class of the source of the time-series.

Table 1: We list here the time series features we used with random forest. This *dmdt* approach was developed for use in optical astronomy, where it is traditional to use magnitudes (proportional to $-1 \times \log(\text{flux})$) for the calculations so that a greater range could be accommodated. In the astronomy case, *mag* refers to the measured values of the observable and flux is calculated as $10^{-0.4 \times \text{mag}}$. In this paper, we have re-purposed the approach treating the measured amplitudes like astronomical magnitudes, and for values corresponding astronomical flux in the *dmdt* approach, we took the exponential of the measured amplitude ($e^{\text{amp}} = 10^{-0.4 \times \text{amplitude}}$).

Feature	Formula
mean	$\langle \text{amplitude} \rangle$
min	amplitude_{\min}
max	amplitude_{\max}
halfpeak2peak	$0.5 * (\text{amplitude}_{\max} - \text{amplitude}_{\min})$
beyond1std	$p((\text{amplitude} - \langle \text{amplitude} \rangle) > \sigma)$
percentile ratio mid20	$(e_{60}^{\text{amp}} - e_{40}^{\text{amp}}) / (e_{95}^{\text{amp}} - e_5^{\text{amp}})$
percentile ratio mid35	$(e_{67.5}^{\text{amp}} - e_{32.5}^{\text{amp}}) / (e_{95}^{\text{amp}} - e_5^{\text{amp}})$
percentile ratio mid50	$(e_{75}^{\text{amp}} - e_{25}^{\text{amp}}) / (e_{95}^{\text{amp}} - e_5^{\text{amp}})$
percentile ratio mid65	$(e_{82.5}^{\text{amp}} - e_{17.5}^{\text{amp}}) / (e_{95}^{\text{amp}} - e_5^{\text{amp}})$
percentile ratio mid80	$(e_{90}^{\text{amp}} - e_{10}^{\text{amp}}) / (e_{95}^{\text{amp}} - e_5^{\text{amp}})$
linear trend	b where $\text{amplitude} = a * t + b$
max slope	$\max((\text{amplitude}_{i+1} - \text{amplitude}_i) / (t_{i+1} - t_i))$
median absolute deviation	$\text{med}(e^{\text{amp}} - e_{\text{med}}^{\text{amp}})$
median buffer range percentage	$p(e^{\text{amp}} - e_{\text{med}}^{\text{amp}} < 0.1 * e_{\text{med}}^{\text{amp}})$
pair slope trend	$p(e_{i+1}^{\text{amp}} - e_i^{\text{amp}} > 0; i = n - 30, n)$
percent difference percentile	$(e_{95}^{\text{amp}} - e_5^{\text{amp}}) / e_{\text{med}}^{\text{amp}}$

described in [31] to be sufficient for our targeted problem. Figure 2 shows a schematic of the transformation from a time-series to features to classifications.

2.2.2. Convolutional neural networks A convolutional neural network (CNN; [32, 24]) is a supervised method of classification belonging to the deep artificial neural network class of machine

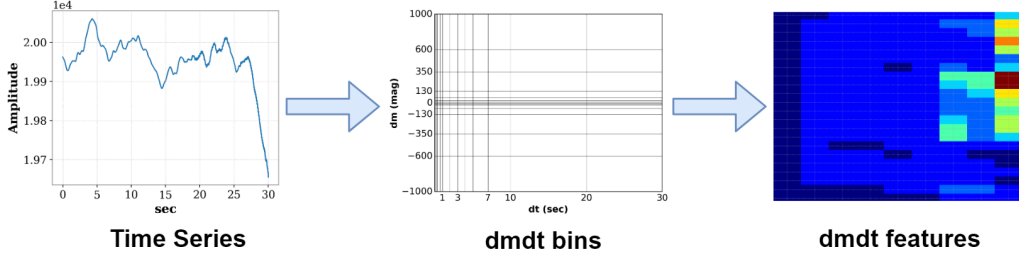


Figure 3: Converting a time-series into a *dmdt* mapping. The left panel is the time-series, the middle panel shows the *dmdt* bins, and the third is the *dmdt* embedding where unequal sized *dmdt* bins are converted to equal-sized pixels. Following [31], here *dm* is the negative log of auxiliary channel time-series amplitude.

learning algorithms. A CNN is an extension of artificial neural network (ANN) and like an ANN it consists of an input layer (typically 2D), an output layer, and multiple hidden layers. The main difference is that it works on smaller parts of an image at a time through kernels and thus there can be translational independence, and at the same time processing of an image can be distributed over several processors of a GPU. The number of layers can also be greater giving rise to the name *deep network*.

We included CNNs, which require images as input, in our analysis due to a similar successful application to astronomical light curves (time series) [33]. In this method, the time-series is converted to a 2D representation (called *dmdt*) by considering all pairwise differences in time (*dt*) and the observable (*dm*), followed by the binning of the differences over a range of defined *dm* and *dt* intervals. The 2D plot so obtained is called a *dmdt*-image (see Figure. 3). These images are then used to train a ConvNet for classification. The original *dmdt* approach used the negative log of flux, the magnitude, of light curves for (*dm*). For this study, we used the observed values for auxiliary channels as “flux” in calculating *dm*.

In addition to the *dmdt*-images, we also used spectrograms, another image representation of the time-series. Spectrograms are two-dimensional time-frequency decompositions of a time series that represent the amplitude of the data over both time and frequency. We consider both median-normalized spectrograms, where the data in each time and frequency bin normalized to the median amplitude for the corresponding frequency bin, and unnormalized spectrogram as features for a CNN. Figure 5 shows the workflow of transforming time-series to *dmdt* images and spectrograms for CNN classification.

2.2.3. *t*-embedded stochastic neighbour embedding *t*-distributed Stochastic Neighbor Embedding (t-SNE; [30]) is a non-linear dimensionality reduction technique used for the visualization of high dimensional data into 2 or 3 dimensions. In this study, we used t-SNE to identify unsupervised clusters given *dmdt* features for each considered auxiliary channel, as shown in Figure 6. We compared the clustered output to labeled lockloss intervals and normal operation intervals (‘quiet’ hereafter) to provide an indication of whether a given channel can capture lockloss activity and is able to distinguish it from quiet times. If quiet times form a single cluster while the lockloss intervals form two to three clusters, this may indicate different causes for lockloss. *Perplexity* sets the number of effective nearest neighbors. We experimented with a variety of perplexity values of

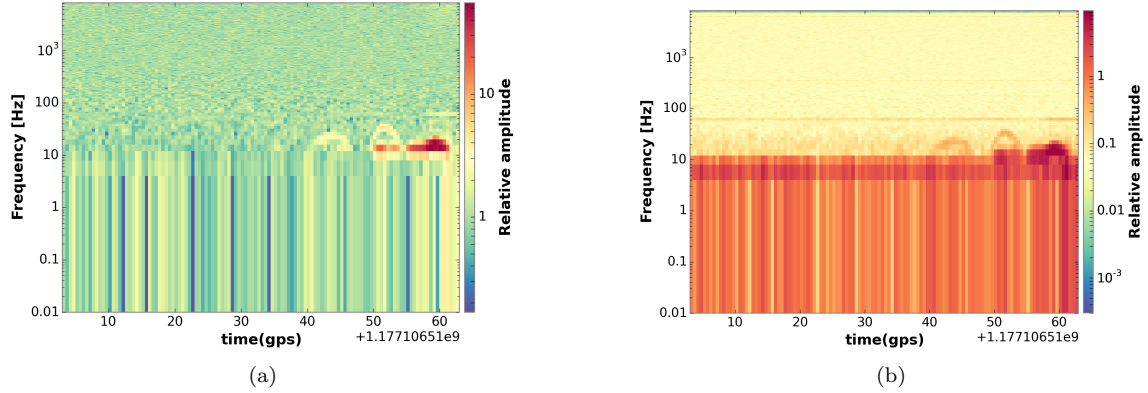


Figure 4: Examples of LIGO auxiliary channel spectrograms generated for CNN classification. Median-normalized spectrogram (left) and unnormalized spectrogram (right) of duration 30 seconds for SRCL channel. These spectrograms were produced using a time bin width of 0.25 seconds, PSDs generated using an fft-length of 0.5 seconds, and overlap between PSD estimations of 50%.

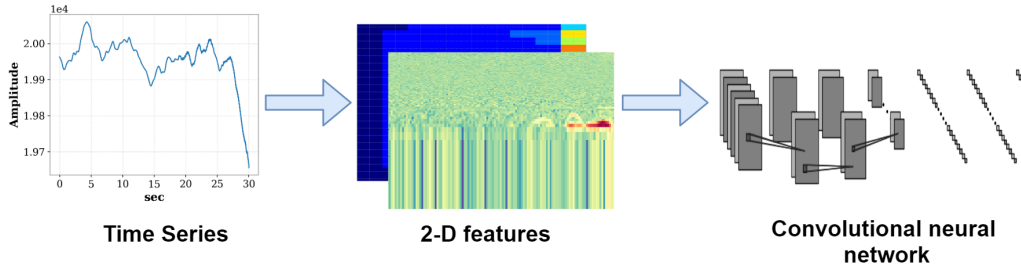


Figure 5: Work-flow for CNN classification. The left panel shows a time-series before conversion to a *dmdt*-image and spectrogram, as show in the middle panel. These images are fed to CNNs for supervised classification. Once trained, the CNN can then be used in real-time or in archival mode to classify incoming time-series to predict possible lockloss events.

2, 5, 10, 20, 60, and 100 for 2000 iterations with a learning rate of 200. We found that t-SNE was not effective in clustering spectrograms, and we did not pursue that further.

We used the Scikit-learn library [34] for implementing random forest and t-SNE. We used Keras [35] with a tensorflow [36] backend for training CNNs.

2.3. Event selection

For labelled lockloss times, we used the *Guardian* state machine platform [37] to identify 942 times when the LIGO-Hanford detector transitioned to the lockloss state during O2. We excluded any lockloss event that occurred within 5 minutes of another lockloss event. Additionally, we identified 1094 quiet times in observation mode which were at least 4 minutes away from lockloss events. We reserved 25% of lockloss and quiet time examples as a test set and we used the remaining examples for constructing the training set.

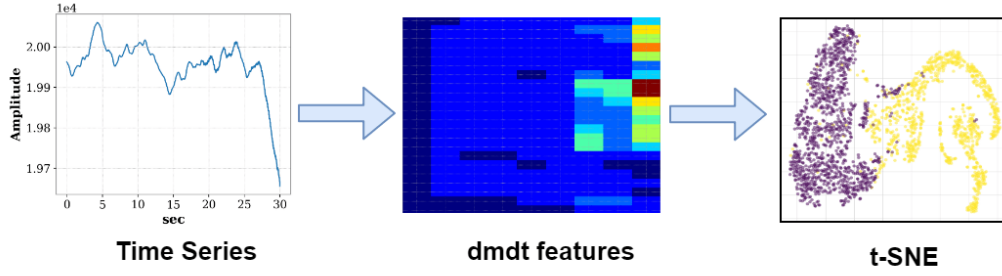


Figure 6: Work-flow for t-SNE. Time series (left panel) are converted to *dmdt*-images (middle panel) and these form input to t-SNE (example in the right panel). While t-SNE is unsupervised, we applied known labels (yellow and purple) to clustered output to investigate the effectiveness of each channel in accurately distinguishing lock losses from quiet times.

We analyzed the minimum time duration prior to lockloss that captured the variance of the channel for different types of channels. For channels monitoring the sensing and control of the interferometer optic cavities, we used a duration of 30 seconds prior to lockloss. For 0.03-0.1 Hz ground motion, where we would expect earthquake and wind event to be most evident, we used a duration of one hour. For 0.1-0.3 Hz ground motion, where microseismic ground motion dominates, we used a duration of 24 hours. For 10-30 Hz ground motion, which witnesses ground motion induced by human activity, we used a duration of 10 minutes.

2.4. Optimizing *dmdt* features

In order to maximize the performance of the convolutional neural net, we optimized our chosen feature set to best capture the behavior exhibited by our selected auxiliary channels prior to loss of lock. Here we outline our procedure for determining the best approach for conditioning the time series data we projected onto the *dmdt* feature space, and deciding the binning (*dm* and *dt* bins) for the *dmdt* features. We used strong earthquake times (0.03-1 Hz ground motion velocity > 500 nm/s) when we expected to see a resulting loss of lock in order to isolate frequency ranges where auxiliary channels exhibited a response to the elevated ground motion prior to the lockloss event. We repeated this procedure for 10 examples to establish a range of channel responses to a strong seismic event.

Down selecting interesting examples For feature set tuning, we compared time-series of the analyzed auxiliary channels to the strain channel for each of the lockloss times corresponding to the 10 selected earthquakes. In some examples, we observed that there is some activity prior to behavior caused by a lockloss, as shown in the top series of plots in Figure 8. We considered such examples in the process of deciding the corner frequencies used for calculating band-limited root-mean-square trends, as described below. We did not consider examples where auxiliary channel behavior was responding to the loss of detector lock (instead of preceding it), as shown in the bottom series of plots in Figure 8.

Deciding corner frequencies for bandpassed *dmdt* features As a distinguishing feature set, *dmdt* is often more effective when a bandpassed time series highlighting only the frequencies that capture the behavior of interest is used as input instead of a raw time series. In order to

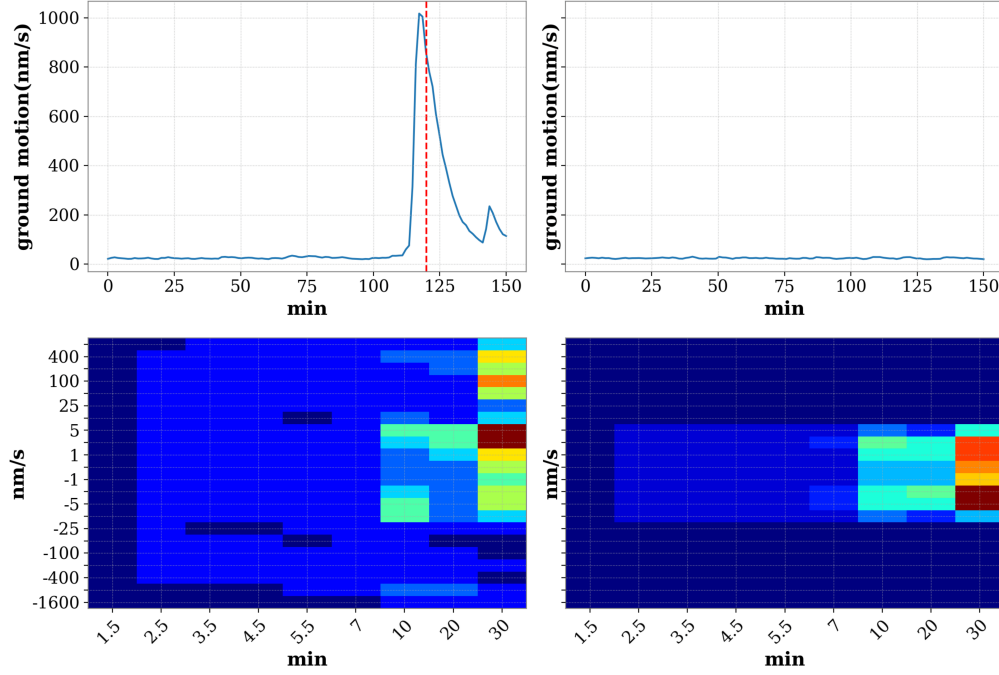


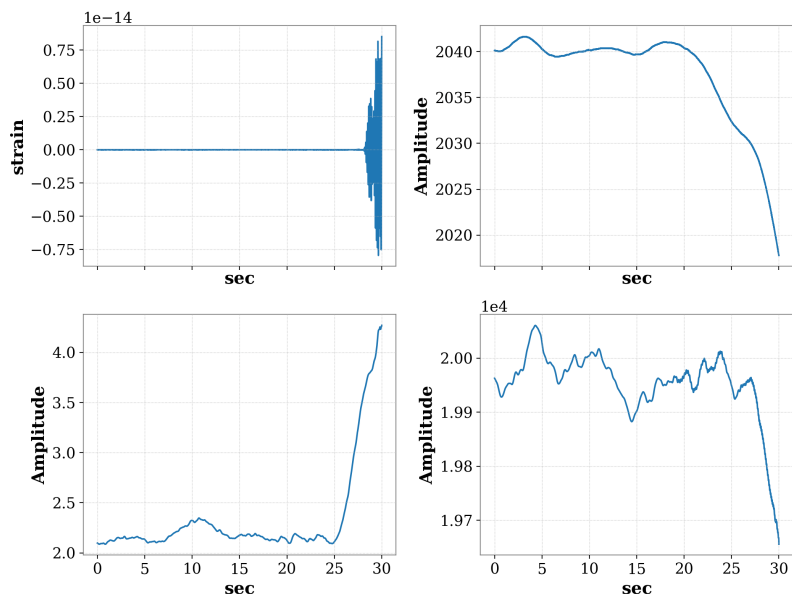
Figure 7: Top left plot is an example of an earthquake with lockloss occurring at the red dashed line. Top right plot is an example of a seismically quiet period. Bottom plots are the corresponding $dmdt$ plots of the above time-series; time: 2017-02-13 07:17:12 UTC, magnitude: 5.3, location: 92 km S of Alaska, distance from H1: 2310.3 km.

determine the frequency band that best captured channel activity prior to lockloss, we evaluated the change in spectral content just prior to lockloss. We visualized this behavior using relative spectra comparing pre-lockloss times and quiet times as well as median-normalized time-frequency spectrograms, as shown in Figure 9. For the ‘pre-lockloss’ spectrum we used 1-5 seconds prior to lockloss, excluding the second just prior to the recorded lockloss in order to avoid contaminating our results with behavior responding to loss of light resonance. For the ‘quiet’ spectrum we used 25-29 seconds prior to lockloss. After selecting the corner frequencies for each of the analyzed channels, we bandpassed and down-sampled the data before passing them to $dmdt$.

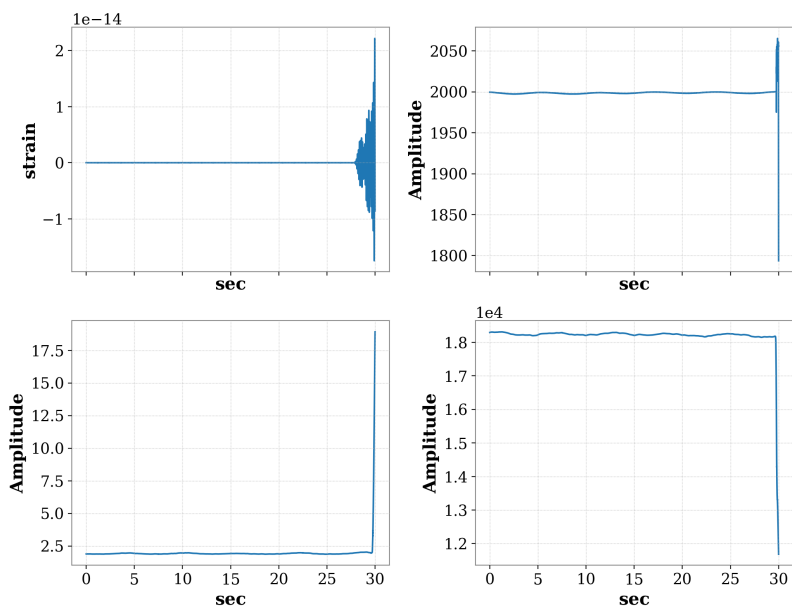
Deciding dm and dt bins We chose dt such that each bin contained at least 10 samples. We distributed dm bins for each channel such that the bins covered the range of differences in magnitude (dm). We ensured that most of the bins are filled while we are able to distinguish between the dm histogram plots of the lockloss and the quiet period. We selected different dm bins for each channel to reflect differences in the base time series magnitude.

3. Results

We analyzed LIGO-Hanford lockloss events during the second Advanced-era observing run (O2) for possible causes. We applied three different machine learning methods, random forests, CNN,



(a)



(b)

Figure 8: For selection of interesting frequency ranges to use to construct distinguishing features, we used lockloss events where auxiliary channels show interesting behavior prior to the lockloss, as shown for the lockloss event on top (2017-01-10 06:36:56 UTC), as opposed to responding to the lockloss, as shown for the event below (2017-01-19 23:11:06 UTC). In the plots, gravitational-wave strain (top-left) and the auxiliary channels IMC (top-right), REFL(bottom-left) and POP(bottom-right) are shown.

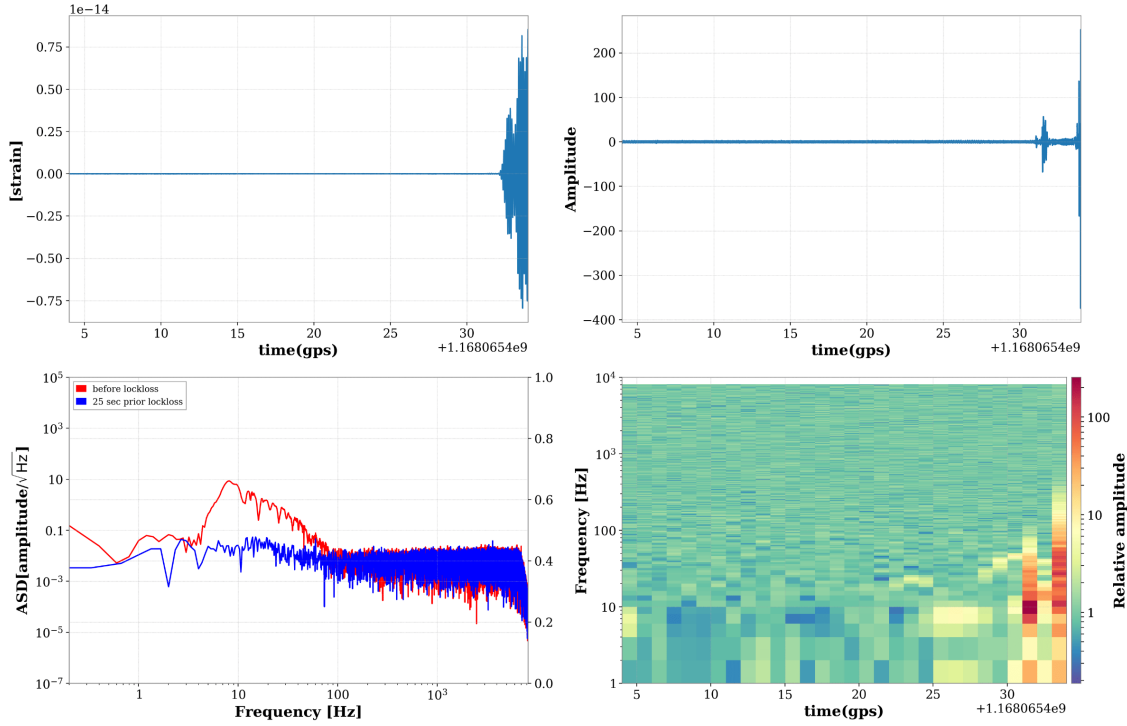


Figure 9: An example of the visualization work flow used to decide the frequency range that best captured behavior prior to lockloss for each analyzed channel. The raw gravitational wave strain time series just prior to a lockloss is shown in the top left plot, where the recorded lockloss occurs at the end of the time series. A raw time series of MICH using same time duration is shown in the top right plot. Relative amplitude spectral densities and a median-normalized spectrogram of MICH are shown in the bottom left and right plots, respectively.

and t-SNE to pre-processed time-series data of a subset of auxiliary channels. We evaluated the computation efficiency of each of the three methods in addition to accuracy with the goal of moving towards a real-time application of the method. All the experiments were performed on Scientific Linux release 7.5 (Nitrogen). Deep learning models were trained on Tesla P4 with 7.4 GB of RAM.

3.1. t-SNE plots

We performed t-SNE on the *dmdt* features of single channels as well as on the combined *dmdt* features of multiple channels where we stacked single channels to form a 3D *dmdt* feature. These results indicate of how well each channel or channel combination can differentiate between lockloss and quiet times. Compared with the CNN method, discussed later in this section, we observe fewer outliers in the t-SNE plots of combined *dmdt*, as shown in Figure 11.

Notably, when we performed t-SNE on the *dmdt* features of environmental ground motion channels, we observe no well defined clusters, as shown in Figure 12. We found that none of the features we derived from the ground motion channels we analyzed, described in Section 2.1, were

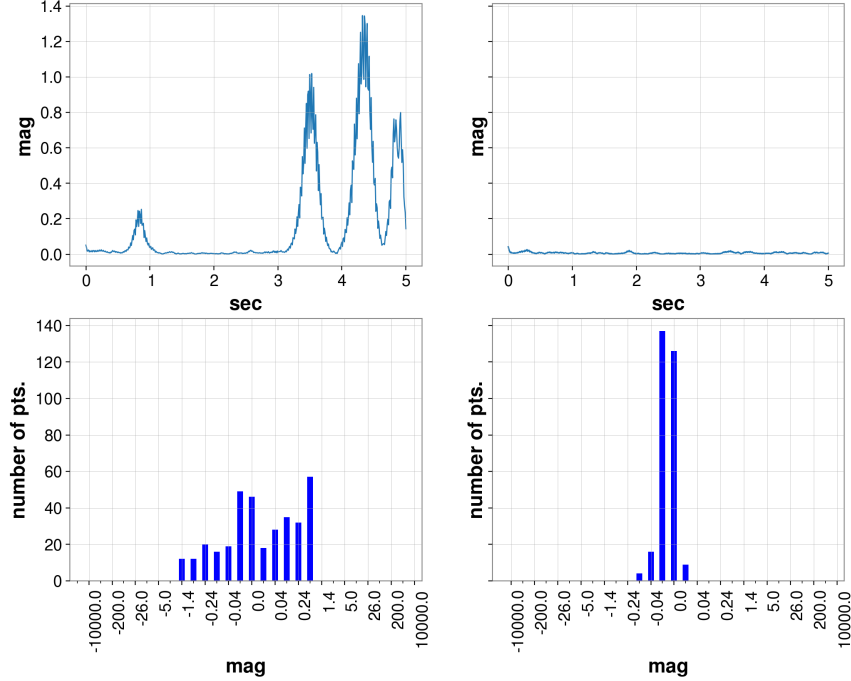


Figure 10: An illustration of how our chosen dm bins capture a lockloss time relative to a quiet time. A lockloss example is shown on the left, and a quiet example on the right. The top plots show a bandpassed time series of LSC-POP, and the bottom plots show dm histograms of that LSC-POP data.

useful distinguishers between lockloss times and quiet times. This result does not contradict the previously reported correlation, on the scale of tens of minutes or more, between seismic events and lockloss events, but it does give strong evidence that interferometer control channels are a much better indicator of when an interferometer is about to lose lock.

3.2. Random forest

We performed binary classification using random forests with features described in Table 1 computed for each of the interferometer sensing and control channels described in Section 2.1. With an analysis of individual channels, we obtained the highest accuracy (92.4%) for the Signal Recycling Cavity Length (SRCL) control channel, as shown in Table 2. This result implicates this element of the interferometer as indicative of a strong majority of lockloss events.

We also analyzed combinations of channels by implementing a soft majority vote, where the vote is decided by taking the mean of probabilities obtained from single channel classification on the random forest classifiers trained on single channels. As shown in Table 3, we obtained a maximum of 95.9% accuracy for a combination of cavity channels.

Confusion matrices for the SRCL channel, the most accurate single channel predictor, and for a combination of all cavity channels are shown in Figure 13. In both cases, true lockloss times are

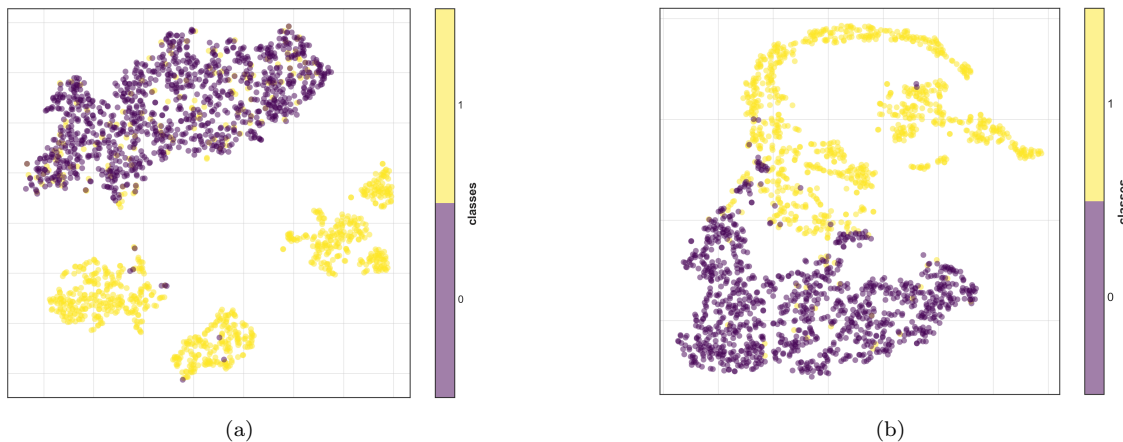


Figure 11: t-SNE clustering of all LIGO-Hanford lock losses during the second observing run (O2). The left plot shows results using only the SRCL channel and the right plot shows results using a combination of multiple channels (LSC-POP+SRCL+MICH). We visualized the accuracy of this unsupervised approach by applying known labels after clustering. Yellow points belong to the lockloss class and purple points belong to the quiet class.

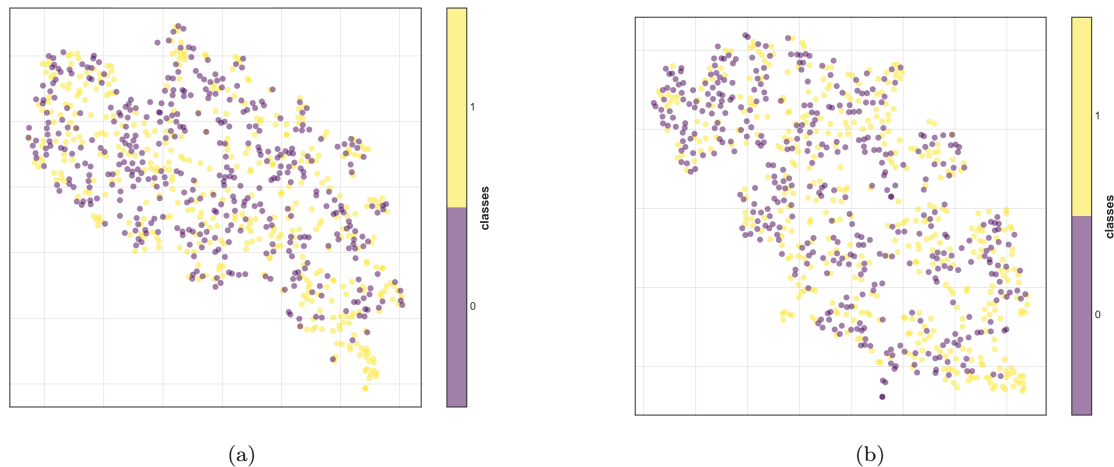


Figure 12: t-SNE on $dmdt$ features of ground motion channels. 0.03-0.1 Hz vertical ground motion, which is useful for capturing earthquake activity, is shown on the left, and 0.03-0.1 Hz horizontal ground motion, useful for capturing wind-induced ground motion, is shown on the right. Ground motion channels show no evidence of clustering into lockloss and quiet times, unlike the interferometer sensing and control channels shown in Figure 11.

Table 2: Random forest on single channels.

Channel	Test accuracy	Matthew's coefficient	F1 score	Specificity	Recall	Precision
MICH	0.902	0.807	0.887	0.964	0.831	0.951
PRCL	0.888	0.787	0.865	0.985	0.775	0.979
SRCL	0.924	0.852	0.911	0.989	0.847	0.985
IMC	0.851	0.714	0.817	0.964	0.72	0.944
POP	0.902	0.806	0.888	0.956	0.839	0.943
REFL	0.898	0.798	0.883	0.956	0.831	0.942

Table 3: Accuracy with soft majority voter on multiple channels.

Channel	Test accuracy	Matthew's coefficient	F1 score	Specificity	Recall	Precision
IMC+POP+REFL	0.912	0.827	0.898	0.974	0.839	0.966
MICH+PRCL+SRCL	0.929	0.865	0.918	0.996	0.852	0.995
All the above	0.959	0.919	0.954	0.996	0.915	0.995



Figure 13: Confusion matrix for random forest classifications: (a) for channel SRCL, (b) for soft majority voter on cavity channels; labels : 0 (quiet), 1 (lockloss).

confused for quiet times more often than vice versa by over a factor of 10.

3.3. CNN with spectrogram

We performed classification with conv-net, as described in Figure 14, on both normalised and unnormalised spectrogram images. We obtain higher accuracy on unnormalised spectrograms than normalised spectrograms. We analyzed sensing and control channels individually, and obtained the highest accuracy (90%) for the MICH channel, as shown in Table 4.

```

Layers = [
  InputLayer,
  Conv2DLayer(16,3x3,ReLU),
  Conv2DLayer(32,3x3,ReLU),
  MaxPoolLayer(3x3),
  DropoutLayer(0.25),
  DenseLayer(16),
  DropoutLayer(0.5),
  DenseLayer(2)
]

```

Figure 14: Layers of the conv-net used for classification of spectrograms.

Table 4: CNN accuracy and loss for single-channel unnormalised spectrograms.

Channel	Test accuracy	Matthew's coefficient	F1 score	Specificity	Recall	Precision
MICH	0.900	0.803	0.885	0.960	0.831	0.947
PRCL	0.851	0.729	0.808	1.000	0.678	1.000
SRCL	0.878	0.758	0.861	0.934	0.814	0.914
IMC	0.825	0.659	0.787	0.938	0.695	0.906
POP	0.853	0.717	0.820	0.964	0.725	0.945
REFL	0.847	0.717	0.805	0.989	0.682	0.982

Table 5: CNN accuracy and loss for multiple-channel unnormalised spectrograms.

Channel	Test accuracy	Matthew's coefficient	F1 score	Specificity	Recall	Precision
IMC+POP+REFL	0.845	0.71	0.804	0.982	0.686	0.97
MICH+PRCL+SRCL	0.888	0.79	0.864	0.993	0.767	0.989
All the above	0.935	0.875	0.926	0.993	0.869	0.99

We also analyzed combinations of channels by feeding the CNN spectrograms of multiple channels. We obtained a maximum accuracy of 93.5% with spectrograms of all six cavity channels as input, as reported in Table 5.

Confusion matrices for the individual MICH channel and the same combination of cavity channels as reported in Table 5 are shown in Figure 15. As with our random forest results, here again we see lockloss events are more likely to be mistaken for quiet times.

3.4. CNN with *dmdt*

We also performed classification with conv-net, as described in Figure 16, on *dmdt* features of single channels. We obtained a maximum accuracy of 92.5% for single channel *dmdt* features with the SRCL channel, as shown in Table 6. Again, this result is similar to individual channel analyses



Figure 15: Confusion matrix for (a) single channel, MICH; (b) cavity channels; labels : 0 (quiet), 1 (lockloss).

```

Layers = [
  InputLayer,
  Conv2DLayer(16,3x3,ReLU),
  Conv2DLayer(32,3x3,ReLU),
  MaxPoolLayer(2x2),
  DropoutLayer(0.25),
  DenseLayer(16),
  DropoutLayer(0.5),
  DenseLayer(2)
]

```

Figure 16: Layers of conv-net for classification with *dmdt*.

that employed random forests and indicates that this single channel can accurately predict most lockloss events.

As with our spectrogram CNN analysis, here we also analyzed combinations of cavity channels by stacking *dmdt* features of multiple channels. We obtained the highest accuracy of all of our attempted approaches, 98.6%, with CNN using stacked *dmdt* features of all six cavity channels reported in Table 7.

Confusion matrices for the individual SRCL channel and the same combination of cavity channels as reported in Table 7 are shown in Figure 17. As with our results for random forests and CNN with spectrograms, here too we see lockloss events are more likely to be mistaken for quiet times.

Table 6: CNN accuracy and loss for single channel *dmdt*.

Channel	Test accuracy	Matthew's coefficient	F1 score	Specificity	Recall	Precision
MICH	0.906	0.816	0.890	0.974	0.826	0.965
PRCL	0.886	0.786	0.861	0.993	0.763	0.989
SRCL	0.925	0.857	0.913	0.993	0.847	0.990
IMC	0.851	0.716	0.816	0.971	0.712	0.955
POP	0.906	0.818	0.889	0.982	0.818	0.975
REFL	0.908	0.823	0.891	0.985	0.818	0.980

Table 7: CNN accuracy and loss for stacked *dmdt* of multiple channels.

Channel	Test accuracy	Matthew's coefficient	F1 score	Specificity	Recall	Precision
IMC+POP+REFL	0.913	0.832	0.900	0.978	0.839	0.971
MICH+PRCL+SRCL	0.968	0.938	0.965	0.996	0.936	0.995
All the above	0.986	0.973	0.985	0.996	0.975	0.996

Figure 17: Confusion matrix for *dmdt* classification;(a) for single channel, SRCL;(b) for stacked *dmdt* of cavity channel; labels: 0 (quiet), 1 (lockloss).

3.5. Obtaining a minimal set of channels for lockloss indicator

We attempt to obtain a small subset of channels which can capture most lockloss activity. For this we derive *dmdt* features from all the channels and train conv-net models on different combination of stacked *dmdt* features. We found that we can achieve an accuracy of 97.5% with MICH and REFL, 98.6% with SRCL, REFL and MICH and around the same with combinations of 4 and 5 channels, as shown in Table 8. We observe the distribution of lockloss events captured by the three best performing channels - SRCL, REFL and MICH. We construct a Venn diagram using the

Table 8: Performance metrics for stacked *dmdt* of multiple channels.

channels	Test accuracy	Matthew's coefficient	F1 score	Specificity	Recall	Precision
SRCL+MICH	0.971	0.941	0.968	0.989	0.949	0.987
POP+MICH	0.971	0.941	0.968	0.985	0.953	0.983
REFL+MICH	0.975	0.949	0.972	0.996	0.949	0.996
POP+MICH+SRCL	0.984	0.969	0.983	1.000	0.966	1.000
REFL+MICH+PRCL	0.984	0.969	0.983	0.996	0.970	0.996
REFL+MICH+SRCL	0.986	0.973	0.985	0.996	0.975	0.996
REFL+MICH+PRCL+SRCL	0.986	0.973	0.985	0.996	0.975	0.996
REFL+MICH+PRCL+IMC	0.986	0.973	0.985	1.000	0.970	1.000
IMC+POP+SCRL+MICH	0.988	0.976	0.987	0.996	0.979	0.996
IMC+POP+SCRL+MICH+PRCL	0.990	0.980	0.989	1.000	0.979	1.000

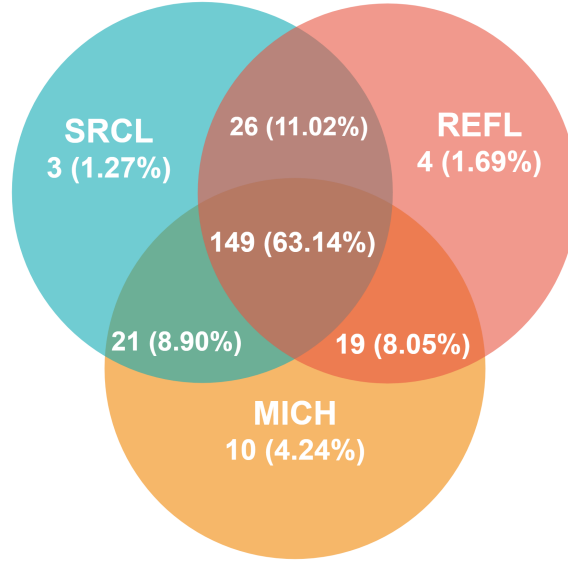


Figure 18: Distribution of lockloss captured by the three chosen cavity channels; Out of 236 test lockloss events, only 4 events could not be captured by any of the three channels.

predictions for the test set events obtained from the models trained on single channel *dmdt* features. We observe that some lockloss events are captured only by a single channel, as shown in Figure 18. Around 63% of events are captured by all the three channels.

3.6. How far in advance can we accurately predict lockloss?

Finally, we try to predict a lockloss event before its occurrence. We derive *dmdt* features from the time-series several seconds before lockloss and perform binary classification to predict whether lockloss occurs or not. We construct separate models for prediction of lockloss at 1, 5, 10, 15, 20

Table 9: Performance metrics for *dmdt* images of the SRCL channel.

Time prior to lockloss (sec)	Test accuracy	Matthew's coefficient	F1 score	Specificity	Recall	Precision
0	0.925	0.857	0.913	0.993	0.847	0.990
1	0.884	0.779	0.861	0.982	0.771	0.973
5	0.778	0.593	0.695	0.978	0.547	0.956
10	0.771	0.579	0.681	0.978	0.530	0.954
15	0.767	0.570	0.676	0.974	0.525	0.947
30	0.765	0.572	0.669	0.982	0.513	0.960

Table 10: Performance metrics for stacked *dmdt* of SRCL+MICH+REFL.

Time prior to lockloss (sec)	Test accuracy	Matthew's coefficient	F1 score	Specificity	Recall	Precision
0	0.986	0.973	0.985	0.996	0.975	0.996
1	0.971	0.941	0.968	0.974	0.966	0.970
5	0.927	0.860	0.916	0.993	0.852	0.99
10	0.916	0.833	0.904	0.964	0.860	0.953
15	0.916	0.834	0.903	0.971	0.852	0.962
30	0.900	0.806	0.882	0.978	0.809	0.970

and 30 secs prior to lockloss. We observe higher accuracies when we use stacked *dmdt* features of multiple channels compared to individual channels. To contrast the performance between single channel and multiple channels, we compare the performance between SRCL (Table 9) and the chosen subset of cavity channels from Figure 18 (Table 10). We observe that in both cases, while the specificity is high for all the times, the predictive accuracy decreases as the time prior to lockloss increases, particularly for single channels. Models trained on stacked *dmdt* features perform quite well with a recall above 85% for time prior to lockloss of less than 15 seconds.

4. Summary and discussion

In this work, we outlined a method to investigate which components within interferometric gravitational-wave detectors are most susceptible to a lockloss using machine learning techniques. We investigated auxiliary channels that formed distinct clusters using the t-SNE approach that accurately distinguished between known quiet and lockloss times. We experimented with different features such as statistical features used with RF, as well as *dmdt* and spectrograms used with CNNs. We found that classification using RF reaches an accuracy comparable CNNs in case of single channel classification. However, classification on stacked *dmdt* features using CNNs outperformed RF in case of multiple channel classification.

In an effort to diagnose the interferometer components associated with locklosses, we identified a minimal subset of channels which captured a majority of lockloss events. We found that a minimal set of three cavity channels (SRCL, REFL and MICH) accurately distinguished between lockloss and quiet times for 98% of the test set examples (232 out of 236 lockless events). We also investigated the performance of our method using a set of channels use to sense and control the

alignment of optical cavities within the LIGO detectors. As reported in Section [Appendix C](#), the accuracy of classification using these alignment channels was found to be lower than the cavity channels discussed above.

We next investigated the power of this approach in predicting a lockloss before it occurs. Using *dmdt* features with a chosen subset of cavity channels, we found the accuracy of this method to be above 90% for times up to 30 seconds prior to lockloss. This result shows extreme promise for applying this method in near-real-time to accurately predict lockloss events before they occur, which may allow automated systems like the Guardian [\[37\]](#) to change the interferometer configuration to avoid a lockloss.

As future work, we intend to improve feature extraction and the overall performance of our method by further analyzing commonalities between mis-classified events, as discussed in Section [Appendix A](#). A further goal is to incorporate a streaming lockloss prediction pipeline for interferometer state changes, complementary to the method described in [\[38\]](#), to increase the duty cycle of the global interferometer network. Another natural extension of this work is to target the diagnosis of data quality artifacts in the data to increase the sensitivity of the transient astrophysical searches.

Acknowledgements

The authors thank Jameson Rollins for useful discussion on other relevant work ongoing within the LIGO Scientific Collaboration and Sheila Dwyer for guidance on auxiliary witnesses that would be fruitful to target for this study. The authors are grateful for computational resources provided by the LIGO Laboratory and supported by National Science Foundation Grants PHY-0757058 and PHY-0823459. AB would like to thank IIT Gandhinagar, the Caltech SURF program, and LIGO, Caltech for support during the study. AM acknowledges support from the NSF (1640818, AST-1815034). AM and JM also acknowledge support from IUSSTF (JC-001/2017). LIGO was constructed by the California Institute of Technology and Massachusetts Institute of Technology with funding from the National Science Foundation, and operates under cooperative agreement PHY-0757058. Advanced LIGO was built under award PHY-0823459. This paper carries LIGO Document Number LIGO-P1900222.

References

- [1] B.P. Abbott et al. GWTC-1: A Gravitational-Wave Transient Catalog of Compact Binary Mergers Observed by LIGO and Virgo during the First and Second Observing Runs. *Preprint*, arXiv 1811.12907, 2018.
- [2] B.P. Abbott et al. GW170817: Observation of Gravitational Waves from a Binary Neutron Star Inspiral. *Phys. Rev. Lett.*, 119(161101), 2018.
- [3] B.P. Abbott et al. Advanced LIGO. *Classical and Quantum Gravity*, 32(7), 2015.
- [4] F. Acernese et al. Advanced Virgo: a second-generation interferometric gravitational wave detector. *Classical and Quantum Gravity*, 32(2), 2014.
- [5] D. Coulter et al. Swope Supernova Survey 2017a (SSS17a), the optical counterpart to a gravitational wave source. *Science*, 358:1556–1558, 2017.
- [6] B.P. Abbott et al. Multi-messenger Observations of a Binary Neutron Star Merger. *Ap. J. Letters.*, 848(2), 2017.
- [7] B.P. Abbott et al. A gravitational-wave standard siren measurement of the Hubble constant. *Nature*, 551:85–88, 2017.
- [8] B.P. Abbott et al. Gravitational Waves and Gamma-Rays from a Binary Neutron Star Merger: GW170817 and GRB 170817A. *Ap. J. Letters.*, 848(2), 2017.

- [9] The LIGO Scientific Collaboration and the Virgo Collaboration. Gravitational-Wave Observatory Status. *The Gravitational Wave Open Science Center (GWOSC)*, https://www.gwopenscience.org/summary_pages/detector_status/, 2019.
- [10] B.P. Abbott et al. Prospects for observing and localizing gravitational-wave transients with Advanced LIGO, Advanced Virgo and KAGRA. *Living Rev. Relativ.*, 21(3), 2018.
- [11] LIGO-Virgo. Gravitational-Wave Candidate Event Database. *gracedb.ligo.org*.
- [12] S. Biscans et al. Control strategy to limit duty cycle impact of earthquakes on the LIGO gravitational-wave detectors. *Classical and Quantum Gravity*, 2018.
- [13] N. Mukund et al. Effect of induced seismicity on advanced gravitational wave interferometers. *Classical and Quantum Gravity*, 36(10), 2019.
- [14] J. Powell et al. Classification methods for noise transients in advanced gravitational-wave detectors. *Classical and Quantum Gravity*, 32, 2015.
- [15] J. Powell et al. Classification methods for noise transients in advanced gravitational-wave detectors II: performance tests on Advanced LIGO data. *Classical and Quantum Gravity*, 34(3), 2017.
- [16] N. Mukund et al. Transient classification in LIGO data using difference boosting neural network. *Phys. Rev. D*, 95, 2017.
- [17] D. George et al. Classification and unsupervised clustering of LIGO data with Deep Transfer Learning. *Phys. Rev. D*, 97, 2018.
- [18] R. Biswas et al. Application of machine learning algorithms to the study of noise artifacts in gravitational-wave data. *Phys. Rev. D*, 88, 2013.
- [19] M. Cavaglia et al. Finding the origin of noise transients in LIGO data with machine learning. *Commun. Comput. Phys.*, 25:963–987, 2019.
- [20] R. Essick et al. *In Prep.*, 2019.
- [21] M. Zevin et al. Gravity Spy: Integrating Advanced LIGO Detector Characterization, Machine Learning, and Citizen Science. *Classical and Quantum Gravity*, 34, 2017.
- [22] S.B. Coughlin et al. Classifying the unknown: discovering novel gravitational-wave detector glitches using similarity learning. *Phys. Rev. D*, 99, 2019.
- [23] N. Mukund et al. Ground motion prediction at gravitational wave observatories using archival seismic data. *Class. Quant. Grav.*, 36(8), 2019.
- [24] Y. A. LeCun et al. Deep learning. *Nature*, 2015.
- [25] A. Effler et al. Environmental influences on the LIGO gravitational wave detectors during the 6th science run. *Classical and Quantum Gravity*, 32(3), 2015.
- [26] P. Covas et al. Identification and mitigation of narrow spectral artifacts that degrade searches for persistent gravitational waves in the first two observing runs of Advanced LIGO. *Phys. Rev. D*, 97, 2018.
- [27] F. Matchard et al. Seismic isolation of advanced ligo: Review of strategy, instrumentation and performance. *Classical and Quantum Gravity*, 32(18), 2015.
- [28] E. J. Daw et al. Long-term study of the seismic environment at LIGO. *Classical and Quantum Gravity*, 2004.
- [29] L. Breiman. Random forests. *Machine Learning*, 2001.
- [30] L. van der Maaten and G. Hinton. User 's Guide for t-SNE Software. *Structure*, 2008.
- [31] J. W. Richards, D. L. Starr, N. R. Butler, J. S. Bloom, J. M. Brewer, A. Crellin-Quick, J. Higgins, R. Kennedy, and M. Rischard. On Machine-learned Classification of Variable Stars with Sparse and Noisy Time-series Data. *The Astrophysical Journal*, 733:10, May 2011.
- [32] Yann LeCun and Yoshua Bengio. The handbook of brain theory and neural networks. chapter Convolutional Networks for Images, Speech, and Time Series, pages 255–258. MIT Press, Cambridge, MA, USA, 1998.
- [33] A. Mahabal et al. Deep-learned classification of light curves. In *2017 IEEE Symposium Series on Computational Intelligence (SSCI)*, pages 1–8, Nov 2017.
- [34] F. Pedregosa et al. Scikit-learn: Machine Learning in Python. *Journal of Machine Learning Research*, 2012.
- [35] F. Chollet. Keras Documentation. *Keras.Io*, 2015.
- [36] M. Abadi et al. TensorFlow: Large-Scale Machine Learning on Heterogeneous Distributed Systems. *None*, 2015.
- [37] J. Rollins. Distributed state machine supervision for long-baseline gravitational-wave detectors. *Review of Scientific Instruments*, 87(094502), 2016.
- [38] M. Coughlin et al. Limiting the effects of earthquakes on gravitational-wave interferometers. *Classical and Quantum Gravity*, 34(4):1–9, 2017.
- [39] Martin Ester, Hans-Peter Kriegel, Jörg Sander, and Xiaowei Xu. A density-based algorithm for discovering clusters a density-based algorithm for discovering clusters in large spatial databases with noise. In *Proceedings of the Second International Conference on Knowledge Discovery and Data Mining, KDD'96*, pages 226–231. AAAI Press, 1996.

Appendix A. Visualizing misclassification

In order to identify how our method could be further improved, we visualized what type of events our CNN approach mis-classified by mapping the probability of the CNN classification with *dmdt* features onto a binary t-SNE unsupervised clustering scale, as shown in Figure A1. We identified some highly localized mis-classified clusters such as the encircled cluster in Figure A1. We isolated the outlier cluster by performing density-based spatial clustering of applications with noise (DBSCAN)[39] on t-SNE output. The outlier cluster is marked 5 in Figure A2. Two examples of timeseries from that cluster shown in Figure A3.

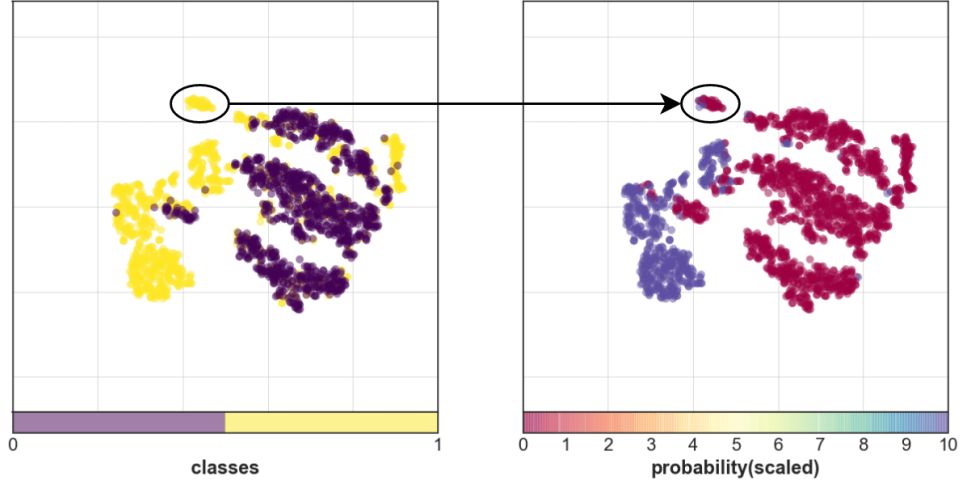


Figure A1: Mis-classification visualization. The left plot shows t-SNE clustering using the *dmdt* features of channel LSC-POP (left). Yellow corresponds to known examples of the lockloss class, and purple to the quiet class. The plot on the right is the same t-SNE plot with the probability mapped from the CNN classification with *dmdt* features, where 0 corresponds to predicted quiet times and 10 to predicted lock losses. The encircled cluster is misclassified by CNN with *dmdt*.

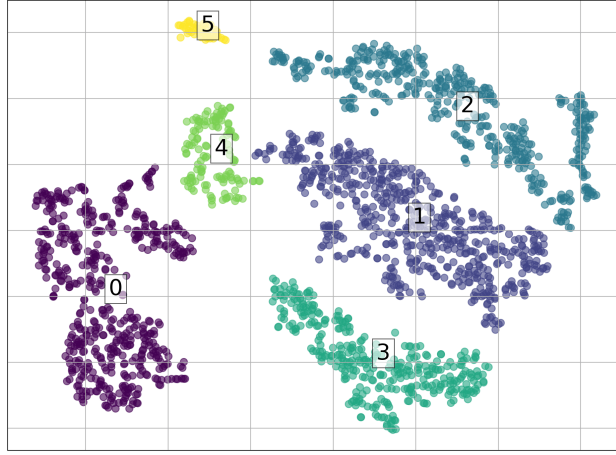


Figure A2: Clustering of t-SNE output using the *dmdt* features of channel POP with DBSCAN into six clusters. The outlier cluster is marked 5 and it contains 43 events. The above plot was generated by keeping the $\epsilon(\text{neighborhood})$ to be 6.

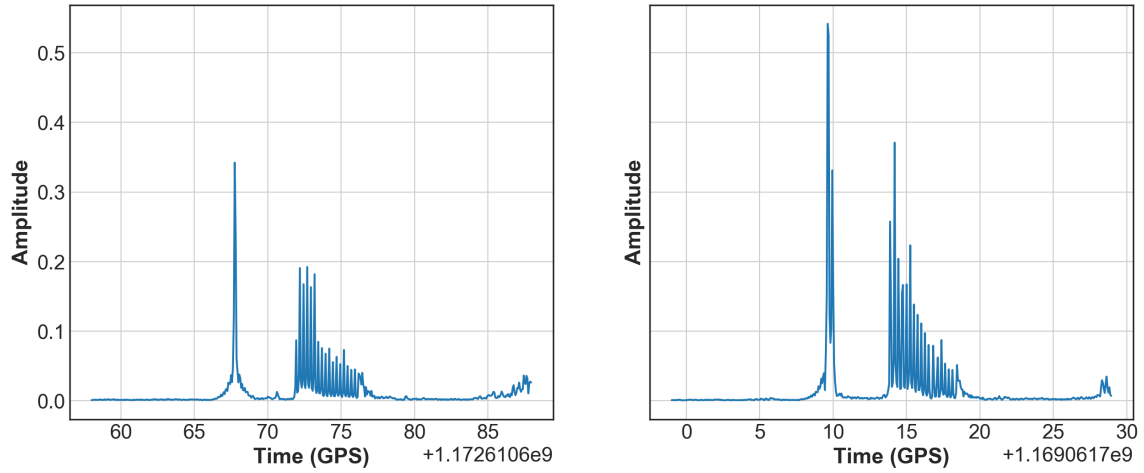


Figure A3: Two examples of bandpassed timeseries of channel POP from the outlier cluster; the left and the right plot are 30 sec time series before the reported lockloss.

Appendix B. Corner frequencies

Table B1: Bandpass frequencies of cavity channels.

Channel	lower cutoff frequency (Hz)	higher cutoff frequency (Hz)
IMC	0.001	30
POP	5	80
REFL	5	100
MICH	0.001	30
PRCL	5	30
SRCL	5	50

Table B2: Bandpass frequencies of ASC channels.

Channel	lower cutoff frequency (Hz)	higher cutoff frequency (Hz)
DC2(P)	1	10
DC3(P)	10	50
DC4(P)	10	50
DC1(Y)	5	20
DC2(Y)	5	20
DC3(Y)	5	20
DC4(Y)	5	50

Appendix C. Results for alignment sensing and control channels

Figure C1: Representative t-SNE results using a single alignment channel (left) and a combination of multiple alignment channels (right). Yellow indicates a known lockloss time and purple a known quiet time. The t-SNE perplexity used here is 20.

Table C1: Performance metrics for Random Forest using single channels.

Channel	Test accuracy	Matthew's coefficient	F1 score	Specificity	Recall	Precision
DC2(P)	0.869	0.745	0.842	0.963	0.758	0.947
DC3(P)	0.904	0.815	0.886	0.985	0.809	0.979
DC4(P)	0.894	0.800	0.872	0.993	0.780	0.989
DC1(Y)	0.869	0.746	0.842	0.967	0.754	0.952
DC2(Y)	0.882	0.770	0.862	0.96	0.792	0.944
DC3(Y)	0.886	0.780	0.864	0.974	0.784	0.964
DC4(Y)	0.906	0.822	0.887	0.996	0.801	0.995

Table C2: Performance metrics for Random Forest using multiple channels; ASC-pitch : DC2(P)+DC3(P)+DC4(P) and ASC-yaw : DC1(Y)+DC2(Y)+DC3(Y)+DC4(Y).

Channel	Test accuracy	Matthew's coefficient	F1 score	Specificity	Recall	Precision
ASC-pitch	0.908	0.827	0.889	1.000	0.801	1.000
ASC-yaw	0.896	0.806	0.874	1.000	0.775	1.000
All the above	0.900	0.813	0.879	1.000	0.784	1.000



Figure C2: Confusion matrix for random forest classification: (a) for single channel, DC4(Y);(b) for multiple ASC channels(pitch); labels: 0 (quiet), 1 (lockloss).

Table C3: Performance metrics for CNN using single channel spectrograms.

Channel	Test accuracy	Matthew's coefficient	F1 score	Specificity	Recall	Precision
DC2(P)	0.841	0.706	0.796	0.989	0.669	0.981
DC3(P)	0.869	0.749	0.840	0.974	0.746	0.962
DC4(P)	0.873	0.759	0.843	0.985	0.742	0.978
DC1(Y)	0.843	0.698	0.807	0.96	0.708	0.938
DC2(Y)	0.845	0.719	0.799	1.000	0.665	1.000
DC3(Y)	0.859	0.742	0.820	1.000	0.695	1.000
DC4(Y)	0.861	0.730	0.832	0.960	0.746	0.941

Table C4: Performance metrics for CNN using multiple channel spectrograms.

Channel	Test accuracy	Matthew's coefficient	F1 score	Specificity	Recall	Precision
ASC-pitch	0.839	0.684	0.808	0.934	0.729	0.905
ASC-yaw	0.855	0.735	0.814	1.000	0.686	1.000
All the above	0.847	0.704	0.813	0.956	0.720	0.934



Figure C3: Confusion matrix for spectrogram classification: (a) for single channel, DC4(P);(b) for stacked *dmdt* of ASC channels(yaw); labels: 0 (quiet), 1 (lockloss).

Table C5: Performance metrics for CNN using a single channel *dmdts*.

Channel	Test accuracy	Matthew's coefficient	F1 score	Specificity	Recall	Precision
DC2(P)	0.867	0.745	0.837	0.974	0.742	0.962
DC3(P)	0.902	0.815	0.882	0.996	0.792	0.995
DC4(P)	0.906	0.823	0.887	1.000	0.797	1.000
DC1(Y)	0.863	0.741	0.830	0.982	0.725	0.972
DC2(Y)	0.849	0.711	0.814	0.967	0.712	0.949
DC3(Y)	0.882	0.771	0.860	0.967	0.784	0.954
DC4(Y)	0.890	0.789	0.869	0.978	0.788	0.969

Table C6: Performance metrics for CNN using combination of multiple channels *dmdt*; ASC-pitch : DC2(P)+DC3(P)+DC4(P) and ASC-yaw : DC1(Y)+DC2(Y)+DC3(Y)+DC4(Y).

Channel	Test accuracy	Matthew's coefficient	F1 score	Specificity	Recall	Precision
ASC-pitch	0.892	0.789	0.874	0.964	0.809	0.950
ASC-yaw	0.902	0.812	0.884	0.985	0.805	0.979
All the above	0.910	0.829	0.893	0.996	0.809	0.995



Figure C4: Confusion matrix for *dmdt* classification: (a) for single channel, DC4(P);(b) for stacked *dmdt* of ASC channels(pitch+yaw); labels: 0 (quiet), 1 (lockloss).